

High-resolution nonequilibrium GW calculations based on quantics tensor trains

Maksymilian Środa,¹ Ken Inayoshi,² Hiroshi Shinaoka,² and Philipp Werner¹

¹*Department of Physics, University of Fribourg, 1700 Fribourg, Switzerland*

²*Department of Physics, Saitama University, Saitama 338-8570, Japan*

One of the challenges in diagrammatic simulations of nonequilibrium phenomena in lattice models is the large memory demand for storing momentum-dependent two-time correlation functions. This problem can be overcome with the recently introduced quantics tensor train (QTT) representation of multivariable functions. Here, we demonstrate nonequilibrium GW simulations with high momentum resolution, up to times which exceed the capabilities of standard implementations and are long enough to study, e.g., thermalization dynamics and transient Floquet physics during multi-cycle electric field pulses. The self-consistent calculation on the three-leg Kadanoff-Baym contour employs only QTT-compressed functions, and input functions which are either generated directly in QTT form, or obtained via quantics tensor cross interpolation.

Introduction. The study of nonequilibrium phenomena in correlated lattice systems is an active research field, driven by time-resolved experiments on correlated materials [1], the discovery of nonequilibrium phases with interesting properties [2, 3], and novel theoretical concepts like prethermalization [4, 5] or nonthermal criticality [6, 7]. Since analytical calculations are challenging, numerical simulations play an important role in the analysis of nonequilibrium effects. But they also face severe problems, like the growth of entanglement in density-matrix renormalization group (DMRG) calculations [8, 9] or dynamical sign problems in Monte-Carlo-based techniques [10, 11]. In nonequilibrium Green's function (NEGF) methods [12], a major bottleneck is the memory demand for storing momentum-dependent two-time correlation functions. Even for simple diagrammatic approaches, like second-order lattice perturbation theory [13], the GW method [14, 15], the fluctuation-exchange approximation [16], or the two-particle self-consistent approach [17], this has limited previous simulations to short times and coarse momentum grids.

A recent idea to overcome the memory bottleneck without approximations is to compress the nonequilibrium Green's functions [18]. A low-memory format of particular promise is the quantics-tensor-train (QTT) representation [19]. This approach employs a binary encoding to map the functions onto tensor trains. Previous studies showed that the bond dimensions needed to accurately reproduce two-time Green's functions are moderate [13, 19], so that the QTT representation combines high compression ratios with an exponentially fine resolution of the variables. The latter property can however only be exploited if the simulations (including the input generation) are performed entirely with compressed functions.

Here, we demonstrate nonequilibrium GW calculations based on QTTs for the Hubbard model on the square lattice. Quenched and electric-field driven systems are simulated up to $t_{\max} = 250$ inverse hopping times on a grid of 64×64 \mathbf{k} -points, which is not achievable with a conventional implementation. Furthermore, we show that in physically relevant scenarios the bond dimension only weakly depends on t_{\max} and lattice size.

Model. We focus on the half-filled Hubbard model on an $N_k \times N_k$ square lattice, with the Hamiltonian $H(t) = \sum_{\mathbf{k}\sigma} \epsilon_{\mathbf{k}-\mathbf{A}(t)} c_{\mathbf{k}\sigma}^\dagger c_{\mathbf{k}\sigma} + U(t) \sum_i (n_{i\uparrow} - \frac{1}{2})(n_{i\downarrow} - \frac{1}{2})$. Here, $c_{\mathbf{k}\sigma}^\dagger$ creates an electron with momentum \mathbf{k} and spin σ , $\epsilon_{\mathbf{k}} =$

$-2t_h(\cos k_x + \cos k_y)$ is the electron dispersion, and $n_{i\sigma}$ is the particle-number operator for spin σ and site i . The system is excited either through a time-dependent interaction $U(t)$ or electric field $\mathbf{E}(t)$. The latter is treated via the Peierls substitution, which shifts the dispersion $\epsilon_{\mathbf{k}} \rightarrow \epsilon_{\mathbf{k}-\mathbf{A}(t)}$ by the vector potential $\mathbf{A}(t) = -\int_0^t \mathbf{E}(\bar{t}) d\bar{t}$ [20]. This corresponds to a gauge with vanishing scalar potential. The energy unit is the hopping amplitude $t_h = 1$. We consider paramagnetic states, and suppress the spin index hereafter.

Green's function compression. To study the dynamics, we calculate the interacting contour-ordered Green's function $G_{\mathbf{k}}(t, t') = -i \langle \mathcal{T}_C c_{\mathbf{k}}(t) c_{\mathbf{k}}^\dagger(t') \rangle$, where \mathcal{T}_C is the time-ordering operator on the Kadanoff-Baym contour C [Fig. 1(a)], which runs along $0 \rightarrow t_{\max} \rightarrow 0 \rightarrow -i\beta$ with the maximum time t_{\max} and inverse temperature β [21]. The Green's function is parametrized by 4 components: the Matsubara $G_{\mathbf{k}}^M$, the retarded $G_{\mathbf{k}}^R$, the left-mixing $G_{\mathbf{k}}^L$, and the lesser $G_{\mathbf{k}}^<$ component. Conventional methods [12, 22] represent each of these components as a matrix, after discretization of the contour. Here, instead, each component is a QTT.

Conceptually, the mapping to a QTT proceeds by writing the integers enumerating the discrete time points t, t' as binary numbers $(t_1, \dots, t_R)_2, (t'_1, \dots, t'_R)_2$. $(0, \dots, 0)_2$ represents the first grid point, $t = 0$, whereas $(1, \dots, 1)_2$ the last, $t = t_{\max}$. The matrix is thus reshaped into a $2R$ -way tensor, which is then factorized into a tensor train—a product of $2R$ three-way tensors [Fig. 1(b)]. Its “leg” indices are the binary digits of dimension 2, whereas the dimensions of the auxiliary “bond” indices, D , control both the memory demand and the faithfulness of the factorization. The value of D is set by requiring that the squared Frobenius-norm error at each tensor of the train is less than some cutoff parameter, $|A - \tilde{A}|_F^2 / |A|_F^2 < \epsilon_{\text{cutoff}}$ (A, \tilde{A} mark the accurate and truncated tensors). This gives roughly a $\sqrt{\epsilon_{\text{cutoff}}}$ precision for individual matrix elements. In practice, we never perform the above mapping, but work with compressed objects from the start.

We store $G_{\mathbf{k}}(t, t')$ for each \mathbf{k} -point as 4 QTTs, corresponding to the 4 components. We discretize the contour on an equidistant grid with time step dt on the real- and $d\tau$ on the imaginary-time axis. The grid spacing can be very fine (typically $dt, d\tau \lesssim 10^{-6}$) since the bond dimension of the QTT does

not increase once the grid is fine enough to resolve all relevant scales. Decompressing such a \mathbf{k} -dependent Green's function would use 80.9 exabytes just for the retarded and lesser components ($t_{\max} = 250$, $N_k = 64$ per axis [23]). A more fair comparison to conventional methods, assuming $dt \sim 10^{-2}$, still yields 5.6 terabytes, exceeding the memory of a typical cluster node. In contrast, the QTT-compressed Green's function on the very fine grid needs only 1.1 gigabytes.

GW. The self-consistent *GW* approximation is defined via the real-space self-energy $\Sigma_{ij}(t, t') = iG_{ij}(t, t')\delta W_{ij}(t, t')$, where $G_{ij}(t, t') = (1/N_k^2)\sum_{\mathbf{k}} e^{-i(\mathbf{r}_i - \mathbf{r}_j) \cdot \mathbf{k}} G_{\mathbf{k}}(t, t')$ and $\delta W_{ij}(t, t')$ is the dynamical part of the screened interaction. The full interaction is given by $W_{ij}(t, t') = U_{ij}(t, t') + \delta W_{ij}(t, t')$, where $U_{ij}(t, t') = U(t)\delta_{ij}\delta_C(t, t')$ is the bare interaction with $\delta_C(t, t')$ the contour delta function. We calculate $\delta W_{ij}(t, t')$ from the charge susceptibility $\chi_{ij}(t, t')$ as $\delta W_{ij}(t, t') = U(t)\chi_{ij}(t, t')U(t')$. The susceptibility is obtained from the bosonic Dyson equation $\chi_{\mathbf{k}}(t, t') = P_{\mathbf{k}}(t, t') + [P_{\mathbf{k}} * U_{\mathbf{k}} * \chi_{\mathbf{k}}](t, t')$, where $*$ denotes the contour convolution [21] and $P_{ij}(t, t') = -iG_{ij}(t, t')G_{ji}(t', t)$ is the polarization bubble. The interacting Green's function is computed from the fermionic Dyson equation $G_{\mathbf{k}}(t, t') = G_{0\mathbf{k}}(t, t') + [G_{0\mathbf{k}} * \Sigma_{\mathbf{k}} * G_{\mathbf{k}}](t, t')$. Here, $G_{0\mathbf{k}}(t, t') = -i[\theta_C(t, t') - f_{\beta}(\epsilon_{\mathbf{k}}(0))]e^{-i\int_{t'}^t d\bar{t}\epsilon_{\mathbf{k}}(\bar{t})}$ is the noninteracting Green's function [24], with $f_{\beta}(\omega)$ the Fermi function and $\theta_C(t, t')$ the contour step function [21].

The quantics implementation proceeds as follows.

(i) We prepare the noninteracting $G_{0\mathbf{k}}$ by constructing the 4 QTTs for each \mathbf{k} on the whole contour. In the case of interaction quenches, $\epsilon_{\mathbf{k}}$ is time-independent and $G_{0\mathbf{k}}$ becomes an exponential function (with discontinuity for $G_{0\mathbf{k}}^R$ and $G_{0\mathbf{k}}^M$). Such functions can be represented as QTTs with bond dimension $D = O(1)$ for any contour [19]. In the case of electric-field simulations, we resort to the tensor cross interpolation algorithm [25–29], which prepares the QTT directly by sampling a small number of suitably chosen time points. After obtaining $G_{0\mathbf{k}}$, we use it to calculate $P_{0\mathbf{k}}$ [see step (iv)], which constitutes the ansatz for the charge susceptibility, $\chi_{0\mathbf{k}} = P_{0\mathbf{k}}$.

(ii) We calculate $\Sigma_{\mathbf{k}}$ by Fourier transforming $\chi_{\mathbf{k}} \rightarrow \chi_{ij}$ to obtain the real-space δW_{ij} . With this, we compute Σ_{ij} and transform the result back to momentum space, $\Sigma_{ij} \rightarrow \Sigma_{\mathbf{k}}$.

(iii) We solve the fermionic Dyson equation at each \mathbf{k} . To this end, we reformulate it in terms of 4 Kadanoff-Baym equations and recast those in the form of a linear problem $AX = B$. In short-hand notation, we get $(1 - G_0^M \Sigma^M)G^M = G_0^M$ for the Matsubara and $(1 - G_0^R \Sigma^R)G^R = B^R$ for the real-time components ($\alpha = R,]$), with B^R a constant term that follows from the Langreth rules [12, 30]; see Supplemental Material (SM) [31]. These linear systems are solved by a DMRG-like algorithm, with $O(D^4)$ scaling, that sweeps through the QTT, sequentially updating two tensors at a time.

(iv) We calculate the polarization $P_{\mathbf{k}}$ by Fourier transforming $G_{\mathbf{k}} \rightarrow G_{ij}$, evaluating the bubble, and transforming the result back, $P_{ij} \rightarrow P_{\mathbf{k}}$.

(v) Finally, we solve the bosonic Dyson equation by the

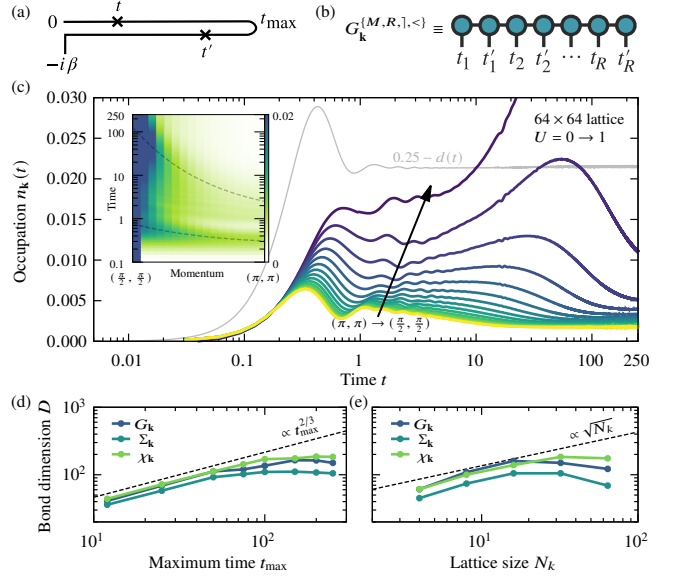


Figure 1. (a) Kadanoff-Baym contour. (b) QTT representation of a Green's function component. (c) Momentum occupations $n_{\mathbf{k}}(t)$ for a $U = 0 \rightarrow 1$ quench and $N_k = 64$, $\beta = 100$. \mathbf{k} is taken along $(\pi, \pi) \rightarrow (\pi/2, \pi/2)$, terminating at the first \mathbf{k} point above the Fermi vector. The inset shows the same data as a color map, with the dashed lines being guides to the eye. The gray line in the main panel plots the change in the double occupation $d(t)$ with respect to the initial value 0.25. (d) Maximum bond dimension D across all components and \mathbf{k} points vs the simulation time t_{\max} . Here, $N_k = 32$. Usually, the lesser component contributes the largest D . (e) The same as in (d) but as a function of linear lattice size N_k with $t_{\max} = 250$. All calculations use $\epsilon_{\text{cutoff}} = 10^{-11}$ in the self-consistency loop.

same method as in (iii).

Steps (ii)-(v) are iterated until self-consistency, i.e., until each (normalized) Green's function component differs between subsequent iterations by $\lesssim 10^{-4}$ - 10^{-3} in terms of the Frobenius norm (see SM [31] for a convergence analysis). We first converge the equations on the Matsubara, and then on the real-time axis. To reduce the computational effort, we restrict the maximum bond dimension D_{\max} in the first iterations and increase it slowly during convergence. In the quench calculations, the accuracy is controlled in late iterations via a fixed ϵ_{cutoff} . To stabilize the equations, we also slowly increase the interaction U .

The elementary operations in our scheme are element-wise multiplications, used to calculate diagrams, and convolutions (matrix multiplications in the discrete form [13, 31]) appearing in the Dyson equation. Both are performed as tensor-network contractions [13, 19], whose computational effort scales as $O(D^4)$ when using the fitting algorithm [32, 33]. There are also 4 Fourier transformations per iteration, to take advantage of the diagonality of the Dyson equation in \mathbf{k} -space and the locality of the diagrams in real-space. We implemented a simple realization of the Cooley-Tukey fast Fourier transform [34], which works on an $N_k \times N_k$ matrix of QTTs, and evaluates QTT sums in the butterfly.

Interaction quench. As a first application, we consider the momentum-dependent relaxation of the Hubbard model after an interaction quench $U = 0 \rightarrow 1$. The system is expected to show a fast relaxation to a prethermalized state, followed by slow thermalization, as found in infinite dimensions [5, 35–37]. We analyze this problem in two dimensions on a 64×64 lattice and up to time $t_{\max} = 250$.

Figure 1(c) presents the momentum occupations $n_{\mathbf{k}}(t) = -iG_{\mathbf{k}}^<(t, t)$ along the diagonal direction $(\pi, \pi) \rightarrow (\pi/2, \pi/2)$. The sudden quench corresponds to a perturbation with wide frequency spectrum, and hence excites electrons up to the highest energies. This high-energy population then relaxes back towards the Fermi level in two waves: a fast one, $t \lesssim 1$, and a slow one, $t \lesssim 100$, with a plateau in between [see the inset of Fig. 1(c)]. During the first wave, a part of the excess kinetic energy is exchanged into interaction energy, but in the second wave these energies are approximately separately conserved. This is shown in gray by the double occupation $d(t)$ (observables defined in SM [31]), which appears to be relaxed to its thermal value already for $t > 1$. The first wave is thus associated with the prethermalization of momentum-averaged quantities, and the second with the actual thermalization. Since potential energy is essentially conserved at late times, the thermalization process converts the high kinetic energy of electrons near $\mathbf{k} = (\pi, \pi)$ into the kinetic energy of many low-energy electronic excitations [5]. This eventually results in a higher-temperature distribution of the final equilibrium state.

The possibility of resolving even longer times depends in particular on how the bond dimension D , which determines the computational effort, scales with the simulation time t_{\max} . In Fig. 1(d), we show D at the last iteration of quench calculations, where it is set only by the truncation cutoff ϵ_{cutoff} . D initially grows as $\sim t_{\max}^{2/3}$ but levels off for $t_{\max} > 100$. Our most expensive operations, solving the Dyson equation and computing the diagrams, scale as $O(D^4)$ in computation time and $O(D^3)$ in memory. If the $t_{\max}^{2/3}$ trend would continue, this would imply a cost $O(t_{\max}^{2.66})$ and $O(t_{\max}^2)$. This is close to that of the conventional methods with $O(t_{\max}^3)$ and $O(t_{\max}^2)$ scaling, albeit in the QTT case likely with smaller prefactors due to the high compression ratios. However, if $D(t_{\max} \rightarrow \infty)$ saturates, as the data suggests, the computational cost for a fixed number of iterations saturates. In reality, while our current implementation outcompetes conventional methods, the number of iterations needed for convergence grows with t_{\max} , and the iteration can become unstable. In the conclusions section, we mention how these issues could be mitigated in the future.

Another relevant scaling for lattice calculations is the bond dimension D vs the lattice size N_k . As shown in Fig. 1(e), D initially grows roughly as $\sqrt{N_k}$ and slows down for $N_k > 32$. This suggests that future implementations of QTT-NEGF methods could benefit from compressing, at least partially [19], also the \mathbf{k} dependence. This could potentially allow to treat exponentially fine \mathbf{k} grids. Furthermore, while the maximum D for $G_{\mathbf{k}}$ in Fig. 1(c) is 122, D averaged over \mathbf{k} is only 8

for the left-mixing, 18 for the retarded, and 50 for the lesser component. While the situation is less favorable for $\Sigma_{\mathbf{k}}, \chi_{\mathbf{k}}$, or in real space, this still provides a gain over conventional methods, which have the same cost for each \mathbf{k} .

Electric-field pulse. As a second application, we study the dynamics induced by an electric-field pulse. The field is polarized along the diagonal direction, $\mathbf{E}(t) = E(t)(1, 1)$, and we choose a box-like pulse $E(t) = E_0 s(t - t_p) \cos(\Omega(t - t_p))$ with envelope $s(t) = 1/((1 + e^{10(t - \delta/2)})(1 + e^{-10(t + \delta/2)}))$. E_0 is the amplitude, Ω the frequency, δ the width, and t_p the pulse center. A continuous ac field renormalizes the hopping amplitude of a noninteracting system as $t_h \rightarrow \mathcal{J}_0(E_0/\Omega) t_h$ [38–40], with \mathcal{J}_0 the zeroth-order Bessel function. In a nonequilibrium situation, where the field is suddenly switched on, this can lead to an inversion of the band structure with a negative-temperature distribution, effectively switching the interaction from repulsive to attractive [41]. To study this behavior, we use a pulse of ~ 15 cycles, a 32×32 lattice and maximum time $t_{\max} = 100$.

Figure 2(a) presents the evolution of the double occupation $d(t)$ during the pulse. For a repulsively interacting half-filled system $d \leq 0.25$, while for an attractively interacting system $d \geq 0.25$. The data thus imply that the pulse indeed inverts the sign of the interaction, which originates in the population inversion, as shown in Fig. 2(b) by the occupation $N(\omega, t)$ [31, 42]. This panel also illustrates the band narrowing effect of the multi-cycle pulse, which here renormalizes the bands by $\mathcal{J}_0(3) \simeq -0.26$, effectively increasing the interaction strength four-fold.

The inverted population has a qualitative effect on the

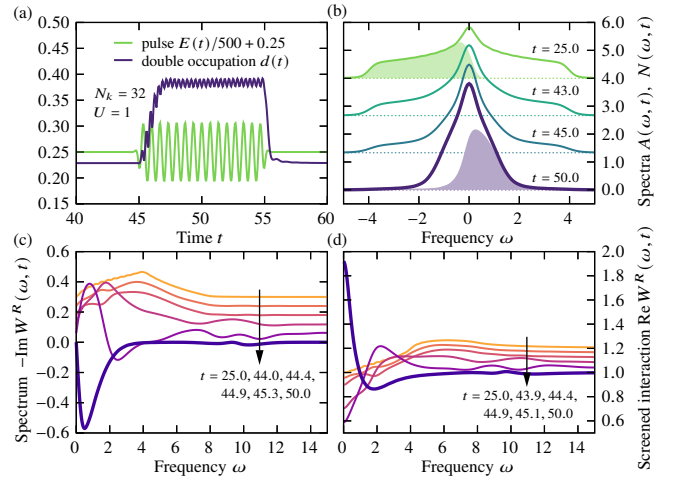


Figure 2. (a) Electric field $E(t)$ ($\Omega = 3\pi$, $E_0 = 3\Omega$) and double occupation $d(t)$. (b) Time dependence of the fermionic spectrum $A(\omega, t)$ (lines) and the occupation $N(\omega, t)$ (shaded regions). (c), (d) Time dependence of $-\text{Im}W^R(\omega, t)$ and $\text{Re}W^R(\omega, t)$. The curves in panel (b) are offset by 1.33, in (c) by 0.06 and in (d) by 0.04. The system parameters are: $U = 1$, $N_k = 32$, $\beta = 10$. The noninteracting Green's function is prepared by tensor cross interpolation with the maximum-norm tolerance 10^{-5} and then truncated with $\epsilon_{\text{cutoff}} = 10^{-8}$. In the self-consistent loop, $\epsilon_{\text{cutoff}} = 10^{-11}$, $D_{\max} = 140$.

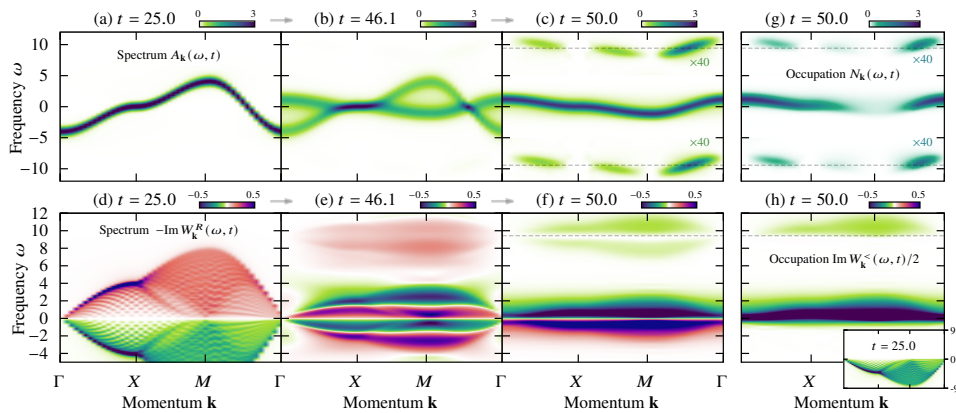


Figure 3. Evolution of (a)-(c) the fermionic spectrum $A_{\mathbf{k}}(\omega, t)$ and (d)-(f) the bosonic spectrum $-\text{Im}W_{\mathbf{k}}^R(\omega, t)$ during an electric-field pulse. (g),(h) Fermionic and bosonic occupations, $N_{\mathbf{k}}(\omega, t)$ and $\text{Im}W_{\mathbf{k}}^<(\omega, t)/2$. The dashed lines in panels (c),(f),(g),(h) mark $\pm\Omega = \pm 3\pi$, where the Floquet subbands appear [in (c),(g), their intensity is multiplied by 40]. The inset in panel (h) plots the bosonic occupation before the pulse. The parameters are the same as in Fig. 2 and the spectra correspond to the gauge with pure vector potential.

screening properties. This is shown in Fig. 2(c), which plots the evolution of $-\text{Im}W^R(\omega, t)$ [31] during the pulse. The shift of the main peak to lower frequencies is again a consequence of the bandwidth renormalization. At $t = 50$, where the inverted population is established, the bosonic spectrum changes sign, indicating an antiscreeing response [see also $\text{Re}W^R(\omega, t)$ in Fig. 2(d)], in agreement with Ref. [43]. In contrast to the dynamical mean-field theory description which neglects nonlocal correlations [41], the GW description of the population-inverted driven state captures two effects that enhance the correlation strength: the bandwidth narrowing and the antiscreeing.

The high momentum and frequency resolution afforded by the QTT method enables a more detailed study of the above physics. Figure 3 shows the evolution of the momentum-resolved fermionic and bosonic spectra, $A_{\mathbf{k}}(\omega, t)$ and $-\text{Im}W_{\mathbf{k}}^R(\omega, t)$ [31]. Before the pulse, the spectra embody the well-known equilibrium dispersions of weakly interacting fermions on a square lattice [Fig. 3(a),(d)]. At the pulse edge, Fig. 3(b), a flipped fermionic band starts forming, leading to a complicated transient state with two dispersions seemingly present (the probe pulse has a width $\delta = 2$, see SM [31]). This is also reflected in the bosonic spectrum [Fig. 3(e)]. Later, during the pulse, the fermionic band completely flips [Fig. 3(c)], and its population is clearly inverted [Fig. 3(g)]. The bosonic subsystem then also evolves into an inverted state, indicated by the sign change of the low-energy contribution to $-\text{Im}W_{\mathbf{k}}^R(\omega, t)$ [Fig. 3(f)]. This inversion is even more directly visible in the bosonic occupation [Fig. 3(h)]. Here, the low-energy contribution shifts from negative (inset) to positive frequencies (main panel). Furthermore, in both the fermionic and bosonic spectra, one can recognize Floquet subbands [40] at multiples of the pulse frequency $n\Omega = n3\pi$, created by electrons that absorb or emit n photons. The occupation of these subbands is also inverted [Fig. 3(g),(h)]. After the pulse, these effects disappear and the system thermalizes at an increased temperature.

Electric-field calculations are more demanding than interaction quenches. Here, the entire calculation uses a fixed D_{\max} , which is slowly increased during convergence up to $D_{\max} = 140$. Moreover, almost all \mathbf{k} points have D saturated

to this value, unlike in the quench setup. We noticed, however, that $D_{\max} \sim 140$ is sufficient to reach the same convergence precision at both $t_{\max} = 50, 100$. This suggests that in the present study, where the system relaxes quickly after the pulse, it is the pulse itself that controls the maximum D . The partitioning of the contour into several QTTs is thus likely to improve the efficiency, as only the subdomain containing the pulse would have a substantial D .

Conclusions. We presented state-of-the-art nonequilibrium GW calculations based on QTTs and demonstrated the potential of this new approach with Hubbard-model simulations on the square lattice. The largest lattices and times we reached were 64×64 and $t_{\max} = 250$, respectively, which would be prohibitively expensive for conventional methods. We also showed evidence that the bond dimension D , controlling the memory demand, saturates with growing t_{\max} and lattice size. It thus appears feasible to simulate even larger systems and longer times with improved implementations, and to essentially overcome the memory bottleneck in lattice simulations.

The main obstacle in the current implementation is the large number of iterations needed for convergence with globally updated Kadanoff-Baym equations and their instability. A promising solution is the application of patching schemes [19], where the Green's functions are partitioned over several small tensor trains defined on subdomains of the contour. Not only does this allow to grow the contour as the calculation proceeds, but it should also further improve the $D(t_{\max})$ scaling. Such a partitioning can be viewed as a generalization of the hierarchical method of Ref. [18] and at least the memory scaling $O(t_{\max} \log t_{\max})$ should be achievable. Judging by the saturation observed here, it could be even better. Since the quantics representation works with exponentially fine grids and in principle allows to compress also the \mathbf{k} -dependence, it is a variant of the hierarchical scheme which promises highly economical and efficient long-time simulations.

Acknowledgements. We thank A. Kauch, M. Ritter, and X. Waintal for helpful discussions. M.Š. and P.W. acknowledge support from SNSF Grant No. 200021-196966. K.I. was supported by JSPS KAKENHI Grant No. 23KJ0883, Japan. H.S. was supported by JSPS KAKENHI Grants No. 22KK0226, and No. 23H03817 as well as JST FOREST Grant No. JP-

MJFR2232 and JST PRESTO Grant No. JPMJPR2012, Japan. The calculations were performed on the beo05 cluster at the University of Fribourg. The QTT-NEGF implementation is written in Julia [44] and is based on the ITensor library [45] and libraries developed by the tensor4all group [29, 46].

-
- [1] C. Giannetti, M. Capone, D. Fausti, M. Fabrizio, F. Parmigiani, and D. Mihailovic, *Advances in Physics* **65**, 58 (2016), <https://doi.org/10.1080/00018732.2016.1194044>.
- [2] T. Kaneko, T. Shirakawa, S. Sorella, and S. Yunoki, *Phys. Rev. Lett.* **122**, 077002 (2019).
- [3] J. Li, D. Golez, P. Werner, and M. Eckstein, *Phys. Rev. B* **102**, 165136 (2020).
- [4] J. Berges, S. Borsányi, and C. Wetterich, *Phys. Rev. Lett.* **93**, 142002 (2004).
- [5] M. Moeckel and S. Kehrein, *Phys. Rev. Lett.* **100**, 175702 (2008).
- [6] J. Berges, A. Rothkopf, and J. Schmidt, *Phys. Rev. Lett.* **101**, 041603 (2008).
- [7] N. Tsuji, M. Eckstein, and P. Werner, *Phys. Rev. Lett.* **110**, 136404 (2013).
- [8] A. J. Daley, C. Kollath, U. Schollwöck, and G. Vidal, *Journal of Statistical Mechanics: Theory and Experiment* **2004**, P04005 (2004).
- [9] S. R. White and A. E. Feiguin, *Phys. Rev. Lett.* **93**, 076401 (2004).
- [10] L. Mühlbacher and E. Rabani, *Phys. Rev. Lett.* **100**, 176403 (2008).
- [11] P. Werner, T. Oka, and A. J. Millis, *Phys. Rev. B* **79**, 035320 (2009).
- [12] G. Stefanucci and R. van Leeuwen, *Nonequilibrium Many-Body Theory of Quantum Systems: A Modern Introduction* (Cambridge University Press, Cambridge, 2013).
- [13] M. Murray, H. Shinaoka, and P. Werner, *Phys. Rev. B* **109**, 165135 (2024).
- [14] D. Golež, P. Werner, and M. Eckstein, *Phys. Rev. B* **94**, 035121 (2016).
- [15] N. Bittner, D. Golež, M. Casula, and P. Werner, *Phys. Rev. B* **104**, 115138 (2021).
- [16] C. Stahl and M. Eckstein, *Phys. Rev. B* **103**, 035116 (2021).
- [17] O. Simard and P. Werner, *Phys. Rev. B* **106**, L241110 (2022).
- [18] J. Kaye and D. Golež, *SciPost Phys.* **10**, 091 (2021).
- [19] H. Shinaoka, M. Wallerberger, Y. Murakami, K. Nogaki, R. Sakurai, P. Werner, and A. Kauch, *Phys. Rev. X* **13**, 021015 (2023).
- [20] R. Peierls, *Z. Physik* **80**, 763 (1933).
- [21] H. Aoki, N. Tsuji, M. Eckstein, M. Kollar, T. Oka, and P. Werner, *Rev. Mod. Phys.* **86**, 779 (2014).
- [22] M. Schüler, D. Golež, Y. Murakami, N. Bittner, A. Herrmann, H. U. Strand, P. Werner, and M. Eckstein, *Computer Physics Communications* **257**, 107484 (2020).
- [23] We employ symmetries to reduce the number of used \mathbf{k} points. We keep $\sim N_k^2/8$ momenta for the quench and $\sim N_k^2/2$ for the electric-field calculations.
- [24] V. Turkowski and J. K. Freericks, *Phys. Rev. B* **71**, 085104 (2005).
- [25] I. V. Oseledets, *SIAM Journal on Scientific Computing* **33**, 2295 (2011).
- [26] S. Dolgov and D. Savostyanov, *Computer Physics Communications* **246**, 106869 (2020).
- [27] Y. Núñez Fernández, M. Jeannin, P. T. Dumitrescu, T. Kloss, J. Kaye, O. Parcollet, and X. Waintal, *Physical Review X* **12**, 041018 (2022).
- [28] M. K. Ritter, Y. Núñez Fernández, M. Wallerberger, J. von Delft, H. Shinaoka, and X. Waintal, *Physical Review Letters* **132**, 056501 (2024).
- [29] Y. N. Fernández, M. K. Ritter, M. Jeannin, J.-W. Li, T. Kloss, T. Louvet, S. Terasaki, O. Parcollet, J. von Delft, H. Shinaoka, and X. Waintal, “Learning tensor networks with tensor cross interpolation: new algorithms and libraries,” (2024), arXiv:2407.02454 [physics.comp-ph].
- [30] D. C. Langreth, “Linear and nonlinear response theory with applications,” in *Linear and Nonlinear Electron Transport in Solids*, edited by J. T. Devreese and V. E. van Doren (Springer US, Boston, MA, 1976) pp. 3–32.
- [31] See Supplemental Material for the full expressions of the Kadanoff-Baym equations, the definition of observables, a convergence analysis, and Ref. [47, 48] not cited in the main text.
- [32] F. Verstraete and J. I. Cirac, “Renormalization algorithms for quantum-many body systems in two and higher dimensions,” (2004), arXiv:cond-mat/0407066 [cond-mat.str-el].
- [33] E. M. Stoudenmire and S. R. White, *New Journal of Physics* **12**, 055026 (2010).
- [34] J. W. Cooley and J. W. Tukey, *Mathematics of computation* **19**, 297 (1965).
- [35] M. Moeckel and S. Kehrein, *Annals of Physics* **324**, 2146 (2009).
- [36] M. Eckstein, M. Kollar, and P. Werner, *Phys. Rev. Lett.* **103**, 056403 (2009).
- [37] M. Stark and M. Kollar, “Kinetic description of thermalization dynamics in weakly interacting quantum systems,” (2013), arXiv:1308.1610 [cond-mat.str-el].
- [38] D. H. Dunlap and V. M. Kenkre, *Phys. Rev. B* **34**, 3625 (1986).
- [39] M. Holthaus, *Phys. Rev. Lett.* **69**, 351 (1992).
- [40] N. Tsuji, T. Oka, and H. Aoki, *Phys. Rev. B* **78**, 235124 (2008).
- [41] N. Tsuji, T. Oka, P. Werner, and H. Aoki, *Phys. Rev. Lett.* **106**, 236401 (2011).
- [42] J. K. Freericks, H. R. Krishnamurthy, and T. Pruschke, *Phys. Rev. Lett.* **102**, 136401 (2009).
- [43] D. Golež, L. Boehnke, H. U. R. Strand, M. Eckstein, and P. Werner, *Phys. Rev. Lett.* **118**, 246402 (2017).
- [44] J. Bezanson, A. Edelman, S. Karpinski, and V. B. Shah, *SIAM review* **59**, 65 (2017).
- [45] M. Fishman, S. R. White, and E. M. Stoudenmire, *SciPost Phys. Codebases*, 4 (2022).
- [46] “Tensor4all,” <https://tensor4all.org>.
- [47] J. Freericks, V. Turkowski, and V. Zlatić, in *HPCMP Users Group Conference* (IEEE Computer Society, Los Alamitos, CA, USA, 2006) pp. 218–228.
- [48] S. R. White, *Phys. Rev. B* **44**, 4670 (1991).

SUPPLEMENTAL MATERIAL

High-resolution nonequilibrium GW calculations based on quantics tensor trains

by M. Środa, K. Inayoshi, H. Shinaoka, and P. Werner

Kadanoff-Baym equations

The Dyson equation reads

$$G(t, t') = G_0(t, t') + [G_0 * \Sigma * G](t, t'), \quad (\text{S1})$$

where $[a * b](t, t') = \int_C d\bar{t} a(t, \bar{t}) b(\bar{t}, t')$ is a convolution on the contour C and the spin and momentum indices are suppressed to simplify the notation. This equation can be viewed as a linear problem by rearranging it as

$$(1 - G_0 * \Sigma *) G = G_0. \quad (\text{S2})$$

By means of the Langreth rules [12, 30], one can also express it in terms of 4 Kadanoff-Baym equations for the Matsubara, retarded, left-mixing, and lesser components. These new equations involve only convolutions on the real- or imaginary-time axes, $[a \cdot b](t, t') = \int_0^{t_{\max}} d\bar{t} a(t, \bar{t}) b(\bar{t}, t')$ and $[a \star b](t, t') = -i \int_0^\beta d\bar{t} a(t, \bar{t}) b(\bar{t}, t')$, respectively. In the integral form and rearranged to reveal the linear-problem structure, they read

$$(1 - G_0^M \star \Sigma^M \star) G^M = G_0^M, \quad (\text{S3})$$

$$(1 - G_0^R \cdot \Sigma^R \cdot) G^R = G_0^R, \quad (\text{S4})$$

$$(1 - G_0^R \cdot \Sigma^R \cdot) G^\Gamma = G_0^\Gamma + G_0^R \cdot \Sigma^\Gamma \star G^M + G_0^\Gamma \star \Sigma^M \star G^M, \quad (\text{S5})$$

$$(1 - G_0^R \cdot \Sigma^R \cdot) G^< = G_0^< + G_0^R \cdot \Sigma^< \cdot G^A + G_0^\Gamma \star \Sigma^\Gamma \cdot G^A + G_0^< \cdot \Sigma^A \cdot G^A + G_0^R \cdot \Sigma^\Gamma \star G^\Gamma + G_0^\Gamma \star \Sigma^M \star G^\Gamma, \quad (\text{S6})$$

where also the usual advanced (A) and right-mixing (Γ) components appear. These components can be reconstructed from the other 4 components by symmetry [21]. Note that the Matsubara component is defined here with an additional i factor, as compared to the usual convention. That is, $G^M(t, t') = -i \langle \mathcal{T}_M c(t) c^\dagger(t') \rangle$, where both arguments lie on the imaginary-time axis and \mathcal{T}_M is a corresponding time-ordering operator. Since the Matsubara equation (S3) defines the equilibrium initial state at $t < 0$, it is decoupled from the rest and can be solved to self-consistency separately as a first step. The remaining equations are solved one by one in the order (S4)-(S6) at each iteration of the self-consistent loop.

In the actual numerical implementation, the equations (S3)-(S6) are discretized. The convolutions thus become matrix multiplications, $[a \cdot b]_{t, t'} = \sum_{\bar{t}} a_{t, \bar{t}} w_{\bar{t}} b_{\bar{t}, t'}$, $[a \star b]_{t, t'} =$

$\sum_{\bar{t}} a_{t, \bar{t}} v_{\bar{t}} b_{\bar{t}, t'}$, where w, v are diagonal matrices containing the integration weights for the real- and imaginary-time axes, respectively. We apply the trapezoidal rule $w = dt \text{diag}(\frac{1}{2}, 1, \dots, 1, \frac{1}{2})$, $v = -id\tau \text{diag}(\frac{1}{2}, 1, \dots, 1, \frac{1}{2})$, which should lead to negligible discretization errors for the very fine grids ($dt, d\tau \lesssim 10^{-6}$) that we use.

Observables

The double occupation is obtained from the contour convolution $\Sigma_{\mathbf{k}} * G_{\mathbf{k}}$ as

$$d(t) = \frac{-i}{N_k^2} \sum_{\mathbf{k}} \frac{[\Sigma_{\mathbf{k}} * G_{\mathbf{k}}]^{<}(t, t)}{U(t)} + 0.25. \quad (\text{S7})$$

The fermionic spectra $A(\omega, t)$, $N(\omega, t)$ and $A_{\mathbf{k}}(\omega, t)$, $N_{\mathbf{k}}(\omega, t)$ are obtained by the following formula for the photoemission intensity [42]

$$I(\omega, t) = \text{Im} \int_0^{t_{\max}} dt_1 \int_0^{t_{\max}} dt_2 S(t_1 - t) S(t_2 - t) e^{i\omega(t_1 - t_2)} \times \mathcal{G}(t_1, t_2). \quad (\text{S8})$$

Here, $I(\omega, t)$ represents the (possibly momentum-resolved) spectrum obtained from a two-time function $\mathcal{G}(t_1, t_2)$, while $S(t) = \exp(-t^2/(2\delta^2))$ is the envelope of the probe pulse with duration δ . We use $\mathcal{G} = G^</(2\pi)$, $-G^R/\pi$ for the occupied $N(\omega, t)$ and full $A(\omega, t)$ spectra, respectively. We take $\delta = 2$ for the momentum-resolved spectra and $\delta = 4$ for the local spectra. The intergral transform (S8) is prepared as a single tensor-train operator by viewing it as two quantum Fourier transforms, which are readily expressible as quantics tensor trains [19]. Note that applying the above formula results in nonnegative fermionic spectra, as physically expected.

The frequency-dependent screened interaction $W^{R, <}(\omega, t)$ [or $W_{\mathbf{k}}^{R, <}(\omega, t)$] is defined via the relative-time Fourier transform,

$$W^{R, <}(\omega, t) = \int dt_{\text{rel}} e^{i\omega t_{\text{rel}}} W^{R, <}(t + t_{\text{rel}}, t - t_{\text{rel}}), \quad (\text{S9})$$

where $t = (t_1 + t_2)/2$, $t_{\text{rel}} = (t_1 - t_2)/2$ are the average and relative times, respectively. The above formula is implemented by first transforming the quantics tensor train into the new variables and then applying a quantum Fourier transform as a tensor-train operator [19]. Additionally, a Gaussian window with standard deviation $\sigma = 10$ is used to reduce ringing artifacts.

Convergence analysis

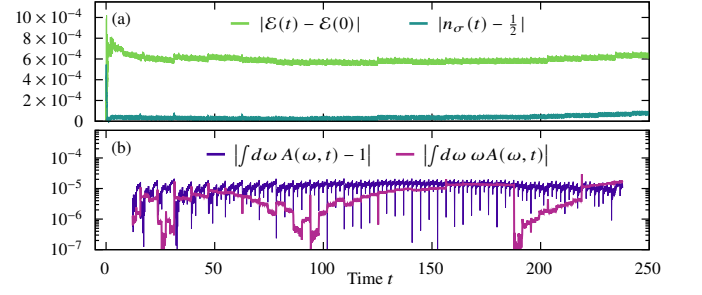
The convergence precision of our nonequilibrium Green's function calculations is measured in terms of the Frobenius-norm difference between subsequent iterations

$$\epsilon_{\text{conv}} = \max_{\mathbf{k}} \sum_{\alpha=R, \downarrow, \uparrow} \frac{|X_{\mathbf{k}, \text{new}}^{\alpha} - X_{\mathbf{k}, \text{old}}^{\alpha}|_{\text{F}}}{|X_{\mathbf{k}, \text{old}}^{\alpha}|_{\text{F}}}. \quad (\text{S10})$$

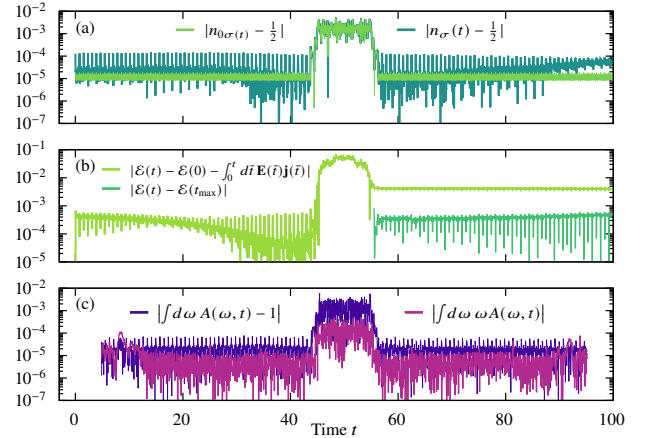
Here, $X = G, \chi$ and it is assumed that $|X_{\mathbf{k}, \text{new}}^{\alpha}|_{\text{F}} \approx |X_{\mathbf{k}, \text{old}}^{\alpha}|_{\text{F}}$, which should be the case close to convergence. We take the maximum across all \mathbf{k} points, so that we can monitor the precision of the most slowly converging \mathbf{k} point. The Frobenius norm is used, as it is the cheapest and most straightforward norm to evaluate with a tensor train. It is also the norm used to measure the faithfulness of the compressed tensor-train representation (see the main text). We are typically converging to $\epsilon_{\text{conv}} \sim 10^{-4}$ - 10^{-3} .

To check whether our convergence criterion is sufficiently strict, we analyze the fermionic sum rules and particle-number and energy conservation at each time instant t . Figure S1 presents such an analysis for the quench results of Fig. 1(c) of the main text. The precision ϵ_{conv} reached in this calculation is $\sim 4.2 \times 10^{-4}$ for the bosonic Dyson equation and $\sim 2.0 \times 10^{-3}$ for the fermionic one. The conservation laws are obeyed up to a similar tolerance. The total energy is conserved up to $\sim 6 \times 10^{-4}$, while the particle number is conserved up to $\sim 1 \times 10^{-4}$ (apart from the initial spikes around $t = 0$). Furthermore, the fermionic sum rules, which are often taken as an adequate convergence check [47], are obeyed up to a higher accuracy, $\sim 1 \times 10^{-5}$. These are satisfactory results which agree with the expectation of about 3 or 4 significant digits of precision, sufficient for the data reported in the main text.

Figure S2 presents an analogous analysis for the electric-field results of Figs. 2 and 3 of the main text. The calculation reached a precision $\sim 5.2 \times 10^{-4}$ for the bosonic Dyson equation and $\sim 2.9 \times 10^{-4}$ for the fermionic one. Here, the conservation laws are well obeyed before and after the pulse, with the particle density $n_{\sigma}(t)$ conserved up to $\sim 10^{-4}$, the energy $\mathcal{E}(t)$ up to $\sim 10^{-3}$, and the sum rules up to $\sim 10^{-5}$. Although during the pulse the deviations are larger, they are still acceptable. These deviations most badly affect the $\int_0^t d\bar{t} \mathbf{E}(\bar{t}) \mathbf{j}(\bar{t})$ integral needed to evaluate the energy conservation in Fig. S2(b). We show, however, that although the value of the energy after the pulse is somewhat inaccurate, the energy is still well conserved, and its difference with respect to the final value $\mathcal{E}(t_{\text{max}})$ is small, $< 10^{-3}$. These additional errors within the pulse duration can be traced back to an inaccuracy present already in the noninteracting $G_{0\mathbf{k}}$ (also the particle density $n_{0\sigma}(t)$ is not very well conserved during the pulse). To fix these issues, one would likely need to impose a smaller tolerance in the tensor cross interpolation algorithm that prepares $G_{0\mathbf{k}}$, and also decrease the singular-value-decomposition cutoff used to truncate $G_{0\mathbf{k}}$ after preparation. This, however, would increase the bond dimension, which is already quite large ($D = 96$) and would make the calculations more demanding. The current



Supplemental Figure S1. Convergence analysis for the quench calculations. (a) Conservation of energy $\mathcal{E}(t)$ and particle density per spin $n_{\sigma}(t)$. (b) Fulfillment of the fermionic sum rules for the zeroth and first moments. For the analysis of sum rules, we evaluate the fermionic spectral function $A(\omega, t)$ with Eq. (S9) instead of Eq. (S8). The first moment is given by $\int d\omega \omega A(\omega, t) = U(\sum_{\sigma} n_{\sigma} - 1)/2$ [48], which evaluates to 0 at half-filling.



Supplemental Figure S2. Convergence analysis for the electric-field calculations. (a) Conservation of particle density per spin: $n_{\sigma}(t)$ is the density for an interacting system, whereas $n_{0\sigma}(t)$ is for the non-interacting one. (b) Conservation of energy $\mathcal{E}(t)$. The electric field $\mathbf{E}(t)$ pumps energy into the system, hence the energy conservation is expressed as $\dot{\mathcal{E}}(t) = \mathbf{E}(t) \mathbf{j}(t)$, where $\mathbf{j}(t) = j(t)(1, 1)$ is the current. After integration, one gets $\mathcal{E}(t) - \mathcal{E}(0) = \int_0^t d\bar{t} \mathbf{E}(\bar{t}) \mathbf{j}(\bar{t})$, which is more convenient to check numerically. We perform the integration on the very fine grid within the quantics-tensor-train format by an appropriate tensor-network contraction. After the pulse, we also show how well the energy is conserved with respect to the final value $\mathcal{E}(t_{\text{max}})$. (c) Fulfillment of the fermionic sum rules for the zeroth and first moments. For the analysis of sum rules, we evaluate the fermionic spectral function $A(\omega, t)$ with Eq. (S9) instead of Eq. (S8). The first moment is given by $\int d\omega \omega A(\omega, t) = U(\sum_{\sigma} n_{\sigma} - 1)/2$ [48], which evaluates to 0 at half-filling.

accuracy is in any case sufficient for the type of data presented in the main text.

The convergence of our solutions on the imaginary axis is also measured with (S10), but for the Matsubara component X^M . The Matsubara equation usually converges to high precision in very few iterations, < 10 , and we hence do not present a detailed convergence analysis.